Impact of Microstructure on the Electron-hole Interaction in Metal Halide Perovskites

Arman Mahboubi Soufiani[1†], Zhuo Yang[2†], Trevor Young[1], Atsuhiko Miyata[2], Alessandro Surrente[2], Alexander Pascoe[3], Krzysztof Galkowski[2,4], Mojtaba Abdi-Jalebi[5], Roberto Brenes[6], Joanna Urban[2], Nan Zhang[2], Vladimir Bulović[5], Oliver Portugall[2], Yi-Bing Cheng[3], Robin J. Nicholas[7], Anita Ho-Baillie[1*], Martin A. Green[1], Paulina Plochocka[2*], Samuel D. Stranks[5,6*]

[1]Australian Centre for Advanced Photovoltaics,
School of Photovoltaic and Renewable Energy Engineering,
University of New South Wales, Sydney, NSW 2052, Australia

[2]Laboratoire National des Champs Magnétiques Intenses, CNRS-UGA-UPS-INSA, 143 Avenue de Rangueil, 31400 Toulouse, France

[3]Department of Materials Science and Engineering, Monash University, Clayton, Vic 3800, Australia

[4]Institute of Experimental Physics, University of Warsaw - Pasteura 5, 02-093 Warsaw, Poland

[5]Cavendish Laboratory, University of Cambridge, J. J. Thomson Avenue, Cambridge CB3 0HE, United Kingdom

[6]Research Laboratory of Electronics, Massachusetts Institute of Technology, Cambridge, MA 02139, United States

[7]Clarendon Laboratory, University of Oxford, Parks Road, Oxford OX1 3PU, United Kingdom

[†] These authors contributed equally to this work.

[*]e-mail:
sds65@cam.ac.uk
paulina.plochocka@lncmi.cnrs.fr
a.ho-baillie@unsw.edu.au

Abstract

Despite the remarkable progress in the performance of devices based on the metal halide perovskite semiconductor family, there is still a lack of consensus on their fundamental photophysical properties. Here, using magneto-optical transmission spectroscopy we elucidate the impact of the microstructure on the Coulomb interaction between photo-created electron-hole pairs in methylammonium lead triiodide ($MAPbI_3$) and the triple-cation lead mixed-halide composition, $Cs_{0.05}(MA_{0.17}FA_{0.83})_{0.95}Pb(I_{0.83}Br_{0.17})_3$ (Cs: Cesium, MA: methylammonium, FA: formamidinium) by investigating thin films with a wide range of grain sizes from tens of nanometers to microns. At low temperatures, in which thermal fluctuations of the interactions are frozen and the rotational disorder of the organic cation is negligible, the exciton binding energy and reduced effective mass of carriers remain effectively unchanged with grain size. We conclude that the microstructure plays a negligible role in the Coulomb interaction of the photo-created electron-hole pairs, in contrast to previous reports. This renewed understanding of the relationship between these fundamental electronic properties and the microstructure is critical for future fundamental studies and improving device design.

Key words: hybrid perovskites, microstructure, exciton binding energy, excitonic reduced effective mass, magneto-optical spectroscopy

Broader context:

Metal halide perovskites such as methylammonium lead iodide ($CH_3NH_3PbI_3$) and alloyed mixed-cation lead mixed-halide counterparts such as $Cs_{0.05}(MA_{0.17}FA_{0.83})_{0.95}Pb(I_{0.83}Br_{0.17})_3$ are creating enormous excitement for their use in high-performance solar cells with potential for exceptionally low capital-intensity for production. An important parameter that dictates the design of a solar cell is the strength of the Coulomb interaction between the photo-generated electron in the conduction band and the hole in the valence band (i.e. the exciton binding

energy). Recently, it has been suggested that the exciton binding energy of the perovskite material is influenced by the size of the grains of the perovskite film, and therefore different device design will be required depending on the grain size. Here, we perform magneto-optic measurements on films with different grain sizes to directly show that the microstructure has a negligible influence on the excitonic properties in the samples, and that excitons do not play a significant role in films with any of the polycrystalline morphologies studied. This means that excitons should not be factor for the design of optoelectronic devices based on polycrystalline $CH_3NH_3PbI_3$ and similar materials with different grain sizes, making future device architecture optimisation less constrained.

Introduction

Solar cells based on lead halide perovskites (with general chemical formula of ABX_3; A = $CH_3NH_3^+$, $HC(NH_2)_2^+$ or Cs^+; B = Pb^{2+} ; X = I^-, Br^- or Cl^-) have achieved astonishingly high power conversion efficiencies exceeding 22% in only seven years since they were first used as sensitizers in photovoltaic solar cells [1-3]. Since then, the remarkable properties of these crystalline semiconductors, such as the tunability of their optoelectronic properties through fabrication of layers with different morphologies, compositions and crystal qualities [4-7], have been further exploited to develop a variety of promising optoelectronic devices [8-11].

As for any emerging semiconductor material deployable in optoelectronic devices, the strength of the Coulomb interaction between the photo-generated electron in the conduction band and the hole in the valence band is of high importance. This was a focus of several studies on perovskites about two decades ago [12-14] and has recently regained attention [15-18] mainly due to the promising outlook of perovskites for solar photovoltaics [10], light-emitting diodes [11] and lasing applications [19] with polycrystalline thin films and single crystals of superior quality than those synthesized two decades ago.

The latest studies have come to a consensus that the exciton binding energy – alternatively known as effective Rydberg (Ry^*) in the Wannier-Mott exciton model – of well-studied $CH_3NH_3PbI_3$ and $CH_3NH_3PbBr_3$ polycrystalline thin films is ~5-12 meV [15, 17, 18] and ~25 meV [16, 18] in the room temperature phase, respectively. These low values, with respect to thermal energy at room temperature ($k_b \times T \approx 26$ meV; k_b is the Boltzmann constant and T is the temperature in Kelvin), are due to generally weak many-body effects (i.e. Coulombic interactions) in these semiconductor systems [20]. Nevertheless, there is ongoing debate concerning the possible tunability of this parameter with variations of the microstructure and hence crystal quality of the perovskite layer [21, 22], being speculated to influence the photo-excited exciton binding energies.

It has been proposed that disordered organic cation dipole domains in small and defective crystals with a large portion of poly-crystallinity can create a large electrostatic potential fluctuation which causes a substantial screening of the photo-generated excitons [22]. This could lead to a very small value of Ry^* on the order of ~2-5 meV [23, 24] meaning that the material behaves as if in the non-excitonic regime. On the other hand, large and defect-free crystals can exhibit an order of magnitude greater values of Ry^* [22, 25]. As a result, one current hypothesis is that it is not possible to assign a universal value to the exciton binding energy of the commonly used $CH_3NH_3PbI_3$ hybrid lead halide perovskites.

A key consequence of this hypothesis could be a change in the working regime (i.e. photo-excited carrier dissociation and transport) of solar cells fabricated from active layers with diverse microstructures. Knowledge of the value of the exciton binding energy is essential because it determines the nature of the majority of the photo-generated species (i.e. free carriers versus excitons) in a semiconductor. For devices comprised of materials with binding energies greater than the probability of thermal dissociation at the working temperature, there would need to be an additional mechanism for exciton dissociation into free carriers, such as

an additional heterojunction, through which they can readily contribute to the photocurrent [26]. In the case that the binding energies are so low that the fraction of photo-excited species that are excitons is negligible, the n- and p-type contacts in the heterojunction structure of the solar cell (cf. most perovskite solar cells) would simply act as charge-selective contacts for the photo-generated electrons and holes, respectively, facilitating simpler device designs. Altogether, these points highlight the need to fully understand the exciton-morphology relationship.

Here, we elucidate the influence of the microstructure, manipulated through the perovskite fabrication method, on the exciton binding energy Ry^* and the excitonic reduced mass (μ) for a variety of $CH_3NH_3PbI_3$ crystal sizes covering the size range reported in devices to date. The impact of the local order and the degree of poly-crystallinity on electron-hole interaction is unraveled through a direct measurement of Ry^* and μ for thin films with different grain sizes. These measurements are performed at low temperature (2 K) at which the impact of $CH_3NH_3^+$ thermal orientational dynamic rearrangement is mitigated. We provide strong evidence that the grain size has negligible influence on the exciton binding energy and effective mass in $CH_3NH_3PbI_3$ and, thus, does not affect the dissociation probability of the bulk excitons and their stability in the photo-excited charge carrier population.

Results and Discussion

Sample Morphology

A wide range of fabrication methods, from single-step [27] to sequential deposition [28] and solution-processed [29] to vapor-assisted [30] techniques, have been employed to fabricate the active layer of perovskite optoelectronic devices in the literature. Here, different deposition methods, which have been shown to give corresponding high-performance solar cells with efficiencies of >16 % [6, 31, 32], are used to controllably tune the perovskite grain size in the

122 films. These samples with $CH_3NH_3PbI_3$ chemical composition but fabricated via different
123 methods with various resulting morphologies simulate the range of different degrees of
124 structural disorder and poly-crystallinity in the $CH_3NH_3PbI_3$ layer in high-performance
125 perovskite devices fabricated to date [22]. The top-view scanning electron microscope (SEM)
126 images of the samples are presented in **Figure 1A-D**. The morphologies vary from a planar
127 polycrystalline film with grain sizes of 772±227 nm [32] (**A**; large grain polycrystalline
128 annotated **LPC**) and polycrystalline film with grain sizes of 214±57 nm [31] (**B**; small grain
129 polycrystalline annotated **SPC**), to small crystals of 291±64 nm fabricated by a two-step
130 dipping technique [6] (**C**; annotated **SC**) and also perovskite infiltrated into a ~2 μm thick
131 mesoporous Aluminum oxide scaffold (mp-Al_2O_3) with grain sizes of <50 nm (**D**; annotated
132 **MP**). As can be seen in the top-view SEM image of the **MP** sample, there is no visible
133 capping layer formed on top of the mesoscopic phase and, therefore, a potential artefact from
134 the larger grain sizes of a capping layer does not influence the related data analysis.

135 ***Magneto-optical Transmission Measurements***

136 Studying the optical behavior of excitons under external fields has proven to be a powerful
137 tool to reveal properties of these quasi-particles in semiconductors [33]. Here, we conducted
138 optical transmission measurements under high magnetic fields (*B*) up to 70T on the samples
139 presented in **Figure 1**. Typical transmission spectra for the large grain polycrystalline thin
140 film sample, showing a strong 1s excitonic transition, are given in **Figure 2A**. For
141 unambiguous identification of the weaker optical transitions, we show in **Figure 2B** the ratio
142 of the transmission spectrum at a specific high magnetic field over the transmission spectrum
143 taken at zero field, illustrating the free-carrier transitions. In **Figure 2C** we show transmission
144 measurements at several monochromatic probe energies under very high magnetic field
145 (<150T) achieved using a short pulse technique. The related spectra for other morphologies
146 are provided in the Supplementary Information, **Figures S1-S3**.

We note that a hydrogen-like excitonic behavior [34] can be assumed for $CH_3NH_3PbI_3$ in the low-temperature orthorhombic phase. The strong minimum in the transmission spectra (**Figure 2A**), attributed to the 1s state of the hydrogen-like free exciton [17], blue shifts with increase of the magnetic field. The second minimum, located at slightly higher energies than the 1s state, is attributed to the first excitonic excited state (labelled as 2s in **Figure 2A)** and also exhibits a blue-shift with magnetic field.

The Landau levels, the free carrier states with quantum numbers N=0,1,2,… formed by quantization of the particle's motion in the plane perpendicular to the magnetic field [33], can be observed at higher energies in the strong magnetic field regime in which $\hbar\omega_c >> Ry^*$ ($\hbar\omega_c = \hbar eB/\mu$), where $\hbar$ and e are Planck's constant and the electron charge, respectively, ω_c is the cyclotron frequency, and $\mu^{-1} = m_e^{-1} + m_h^{-1}$ is the reduced mass of the exciton (m_e and m_h are electron and hole masses, respectively). The free carrier Landau level transitions are dominant at high magnetic fields with transition energy described by $E(B) = E_g + (N + 1/2)\hbar\omega_c$ [16, 17] where E_g is the bandgap. We can then fit the measured optical transitions between Landau levels to extract the reduced mass, μ, independent of the exciton binding energy. The value of the reduced mass thus obtained is used as a fixed parameter in the fit of the hydrogen-like excitonic transitions to extract the exciton binding energy, based on a model which describes the hydrogen atoms in high magnetic field [35]. In this model, a dimensionless parameter γ which is defined as $\gamma = \hbar\omega_c / 2Ry^*$ is used. Makado and McGill calculated the transition energies of excitonic states $E_n(\gamma)$ as a function of quantum number n up to 4 and γ ranging from 0 to 10 [35]. Given values of the magnetic field B and the reduced mass μ, the binding energy Ry^* is the only fitting parameter for the full set of hydrogenic transitions.

The complete set of these excitonic and free carrier transition energies for the **LPC** sample is plotted in the fan diagram in **Figure 2D**. The observation of many Landau levels in the magnetic field <150T allows precise determination of the reduced mass. Knowledge of the reduced mass in turn imposes strong constraints on fitting the excitonic binding energy. An additional influential constraint on the value of the binding energy is set if the higher excitonic transition resonances such as the 2s state are resolved, as for the **LPC** morphology. The observation of a well-resolved 2s state at intermediate magnetic field fixes the transition energy of 2s at zero magnetic field using the model described earlier. The energy separation of 1s-2s at zero magnetic field follows the series of 3D hydrogen-like energy states, $E_n = E_g - Ry^* / n^2$ where E_n is the excitonic transition energy at zero magnetic field. This gives a strong constraint on the exciton binding energy.

The fitting to the hydrogen-like excitonic (dashed lines) and free carrier (solid lines) transitions, as explained in detail in refs. [16, 17, 35], is presented in **Figure 2D** and the Ry^* and μ values for the **LPC** sample are calculated to be 16±1 meV and 0.102±0.002 m_0, respectively. For the morphologies other than **LPC** (i.e. **SPC**, **SC** and **MP**), the identification of free carrier transitions at high energies allows us to obtain the values of the the reduced masses. The extracted μ values are presented in **Table 1** and are very close to the value originally reported by Miyata *et al.* (μ = 0.104±0.003 m_0) [17]. Importantly, we find that the microstructure has negligible influence on the reduced mass. This indicates that the polaron coupling contant, incorporating the effective longitudinal optical (LO) phonon energy and the optical and static dielectric constants of the medium, which couples to the band-edge bare effective masses to form the polaronic masses [18, 36], is only minimally influenced by the variation in microstructure.

In the absence of a clear observation of the 2s excitonic transitions for the **SPC**, **SC** and **MP** samples, the global fit to the full excitonic and free-carrier transitions was employed and the resulting unchanged Ry^* values are presented in **Table 1**. To visualize the negligible change in the optical response under external magnetic fields of the $CH_3NH_3PbI_3$ films with different morphology, the overlaid fan diagrams of the complete set of excitonic and free carrier optical transitions after shifting by the corresponding bandgap offsets are presented in **Figure 3(A)**. Here we clearly show that these $CH_3NH_3PbI_3$ samples, although composed of dramatically different grain sizes and morphologies, exhibit similar magneto-optical behaviour. Furthermore, the XRD patterns (**Figure S4)** show that the $CH_3NH_3PbI_3$ **SPC** and **SC** thin films have some PbI_2 impurities, indicating that the presence of small amounts of PbI_2 also does not affect the excitonic properties of perovskites. We also note that, although the changes in the grain size and morphology do not influence the low-temperature excitonic properties of perovskites, they can affect the optoelectronic response of these materials including their PL behaviour and the fraction of retained tetragonal phase within the orthorhombic phase upon lowering the temperature [37-39].

It was recently shown that when replacing $CH_3NH_3^+$ by a larger monovalent organic cation, formamidinium ($HC(NH_2)_2^+$), the excitonic characteristics of the corresponding perovskite, Ry^* and μ, decreased by less than 15 % [16]. The larger steric size of formamidinium compared to methylammonium results in a larger equatorial bond angle (lead-iodide-lead) and, thus, a narrower optical bandgap [40]. The variation of the crystal size would result in a modified interplay between the organic and the inorganic moieties in the perovskite structure, which in turn changes the strain induced on the crystal structure and thus, impacts the bandgap. The negligible impact on the excitonic characteristics of the degree of dipolar cation order and structural arrangement induced by the variation of perovskite microstructure might be analogous to the small impact of cation substitution on the excitonic properties, with the lead-

halogen sub-unit remaining unchanged in both cases. This indeed demonstrates the critical role of the electronic properties of the inorganic cage in the determination of the excitonic binding energy and reduced effective mass of perovskites. Moreover, this important observation agrees with the recent work by Perez-Osorio *et al*. in which the largest contribution to the static dielectric constant of $CH_3NH_3PbI_3$ was demonstrated to originate from the stretching and rocking vibrational modes of the lead-halogen system rather than the internal modes of the organic cation [41].

Using the values obtained for the effective dielectric constant ($\varepsilon = \sqrt{Ry^H \times \mu / Ry^* \times m_0}$, where Ry^H = 13.6 eV is the Rydberg constant of the hydrogen atom) and the reduced mass, the Bohr radius of the bound electron-hole system can be calculated. This is similar for all the $CH_3NH_3PbI_3$ perovskite morphologies and is about 5 nm in the low temperature phase. The Bohr radius is substantially smaller even than the perovskite crystal size of the **MP** sample and it is consistent with the absence of any signature of a quantum confinement effect on the optical transition of the corresponding excitons in the mesoscopic phase.

The correct interpretation of the optical absorption spectrum for the exciton binding energy derivation in the room temperature tetragonal phase of $CH_3NH_3PbI_3$ (> 160 K) becomes more difficult than in the orthorhombic phase as the large spectral broadening at higher temperatures in the tetragonal phase can potentially mask critical optical transition features even under high magnetic fields [17]. The increased broadening is most likely due to a thermally-induced increase in the orientational disorder and rotational dynamics of the unlocked organic cation above the structural phase transition [42]. The excitonic binding energy has been reported in the literature [17, 18, 24, 43] to decrease upon orthorhombic-to-tetragonal phase transition with a likely reason to be the slight increase in the dielectric constant of the

medium, which is in turn linked to the increase in the effective phonon energy coupling to the carriers.

We argue that the change in the binding energy at the transition to the tetragonal phase for all the morphologies investigated in this study would be similar. This can be partly understood by the dominant influence of thermal disorder on the electrostatic fluctuations at room temperature over the degree of poly-crystallinity and molecular order which are dominant at lower temperatures [22]; the latter properties we have already shown above to have insignificant impact on the electron-hole interaction. This is further supported by a recent theoretical study by Motta *et al.* in which the impact of the degree of molecular dipole orientational disorder – which could be induced by the grain size variation – on the binding energy in the high temperature phase of $CH_3NH_3PbI_3$ was found to be only ~10 % [44].

To generalise our findings for $CH_3NH_3PbI_3$ to other perovskite compositions, we repeat the measurements on a state-of-the-art triple-cation lead mixed-halide perovskite, $Cs_{0.05}(MA_{0.17}FA_{0.83})_{0.95}Pb(I_{0.83}Br_{0.17})_3$ [2]. We consider two significantly different morphologies of this perovskite composition, namely a planar polycrystalline thin film and a film with the perovskite infiltrated into a thick mp-Al_2O_3 scaffold (corresponding SEM images are shown in **Figure S5**). We show in **Figure S6** that both morphologies exhibit similar magneto-optical responses and, thus, similar fundamental excitonic properties, with the binding energy and reduced mass of 13±2 meV and 0.096±0.008 m_0, respectively (see **Table S1**). These results allow us to extend our conclusions to the wider alloyed perovskite family, providing strong evidence that the microstructure has a negligible impact on the excitonic properties in metal halide perovskites.

Recently, Petrozza and co-workers used temperature-dependent time-resolved transient absorption (TA) spectroscopy to track the fate of excitons following photo-excitation and to

understand the relationship between the excitonic properties and film morphology [22]. The conclusion from this study was that the exciton binding energy and, therefore, exciton stability can vary depending on the perovskite film microstructure in the tetragonal phase which is most critical to solar cell operation. Their interpretation was based on the emergence and evolution of the negative feature located at the high-energy end of the photobleach signature in the transmission-difference spectrum, which was attributed to self-renormalization of the exciton energy due to a change in its concentration upon decrease in temperature and/or grain size variation. We note that the negative feature developing in the high-energy tail of the TA spectra over time has been proposed to be primarily a consequence of a bandgap renormalization effect (bandgap narrowing) and of a free carrier absorption, among other possible mechanisms [45, 46]. The spectral TA analysis used in ref. [22], which is an indirect technique for characterising excitonic properties, can also be influenced by recombination mechanisms which are strongly influenced by the perovskite crystal morphology. Furthermore, we note from a previous report for $CH_3NH_3PbBr_3$ perovskite that while Ry^* probably remains unchanged by increasing the temperature from 2 K to room temperature, the increase in the broadening of the linear absorption spectra lessens the 1s transition strength [18, 47]. Although this spectral broadening increase is mainly attributed to thermally-activated mechanisms, a change in the intrinsic broadening of perovskites with different microstructures, due for instance to the difference in their inherent structural disorder, can similarly influence the spectral shape while Ry^* remains unchanged. This makes unambiguous interpretation of the linear and transient absorption spectra difficult when relying on the detection and the strength of the excitonic feature – at the absorption edge – as these techniques are indirect approaches for Ry^* determination compared to the direct approach employed in this study (see **Figure S7** for the zero-field transmission spectra of the four different $CH_3NH_3PbI_3$ morphologies). We note that it is possible there are also transient

changes in excitonic populations and properties (e.g. due to dynamic photo-excited changes in dielectric constant) that will be averaged out in our steady-state measurements.

Conclusions

We investigated the relationship between the excitonic properties and microstructure of the $CH_3NH_3PbI_3$ and $Cs_{0.05}(MA_{0.17}FA_{0.83})_{0.95}Pb(I_{0.83}Br_{0.17})_3$ perovskites using magneto-optical spectroscopy measurements. We find that the microstructure does not influence the excitonic binding energy of $CH_3NH_3PbI_3$ or the broader range of mixed-cation and mixed-halide alloyed compositions. Thus, we conclude that excitons truly play a negligible role in the operation of mixed organic-inorganic metal halide-based perovskites regardless of the thin film deposition technique and final morphology, and that excitons need not be a factor for the design of optoelectronic devices based on polycrystalline $CH_3NH_3PbI_3$ and similar materials with different grain sizes. The universal values of ~16 meV and 0.102-0.109 m_0 for the exciton binding energy and reduced effective mass in the low-temperature phase of $CH_3NH_3PbI_3$ can be used as guidelines for interpretation of the spectroscopic data such as the complex spectra of transient absorption measurements. It also implies that the electronic structure of the inorganic cage – $(PbI_3)^-$ in the case of $CH_3NH_3PbI_3$ – is likely to have the greatest contribution to the excitonic properties of organic-inorganic lead halide perovskites rather than the degree of poly-crystallinity and the order of dipolar organic cation domains.

Figures

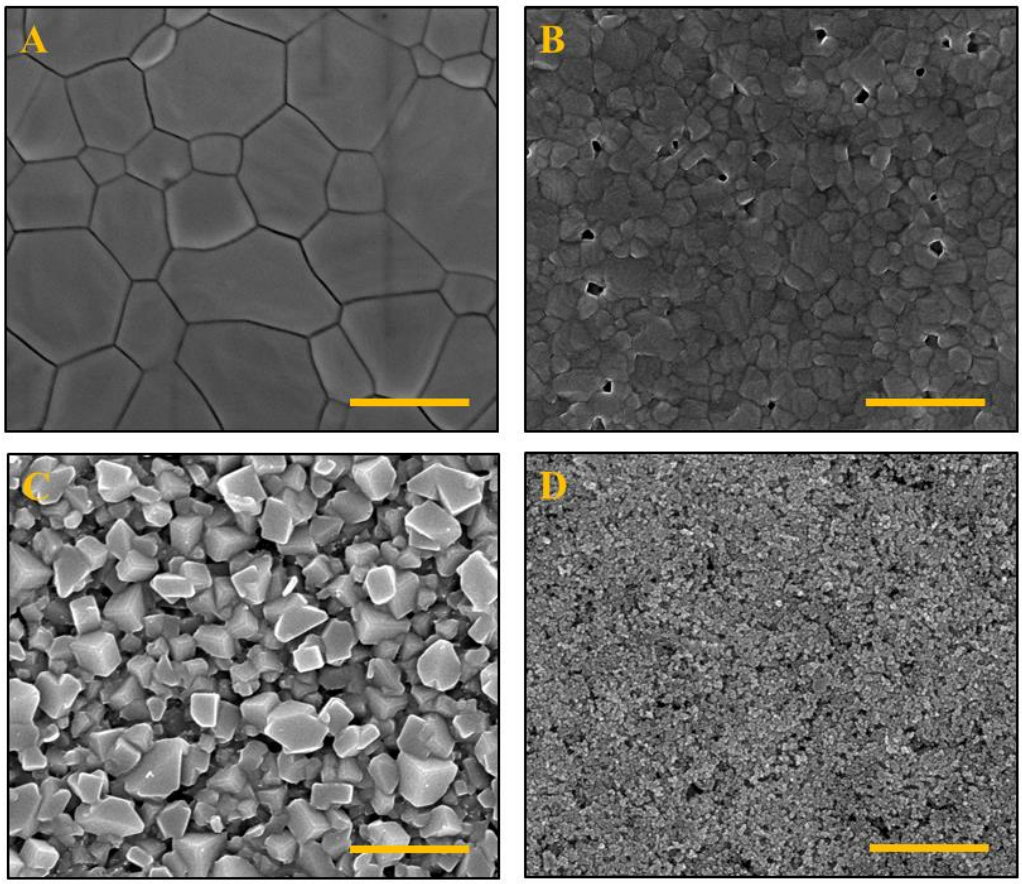

Figure 1 Morphology of $CH_3NH_3PbI_3$ samples. Top-view SEM images of $CH_3NH_3PbI_3$ layer with various morphologies fabricated on glass substrates. **A)** Polycrystalline thin film with grain sizes 772±227 nm (LPC). **B)** Polycrystalline thin film with grain sizes 214±57 nm (SPC). **C)** Small crystals of $CH_3NH_3PbI_3$ fabricated by the two-step solution-processed dipping technique, with resulting crystal sizes 291±64 nm (SC). **D)** $CH_3NH_3PbI_3$ infiltrated into a thick mesoporous-Al_2O_3 scaffold with grain sizes <50 nm (MP). Scale bars are 1 µm.

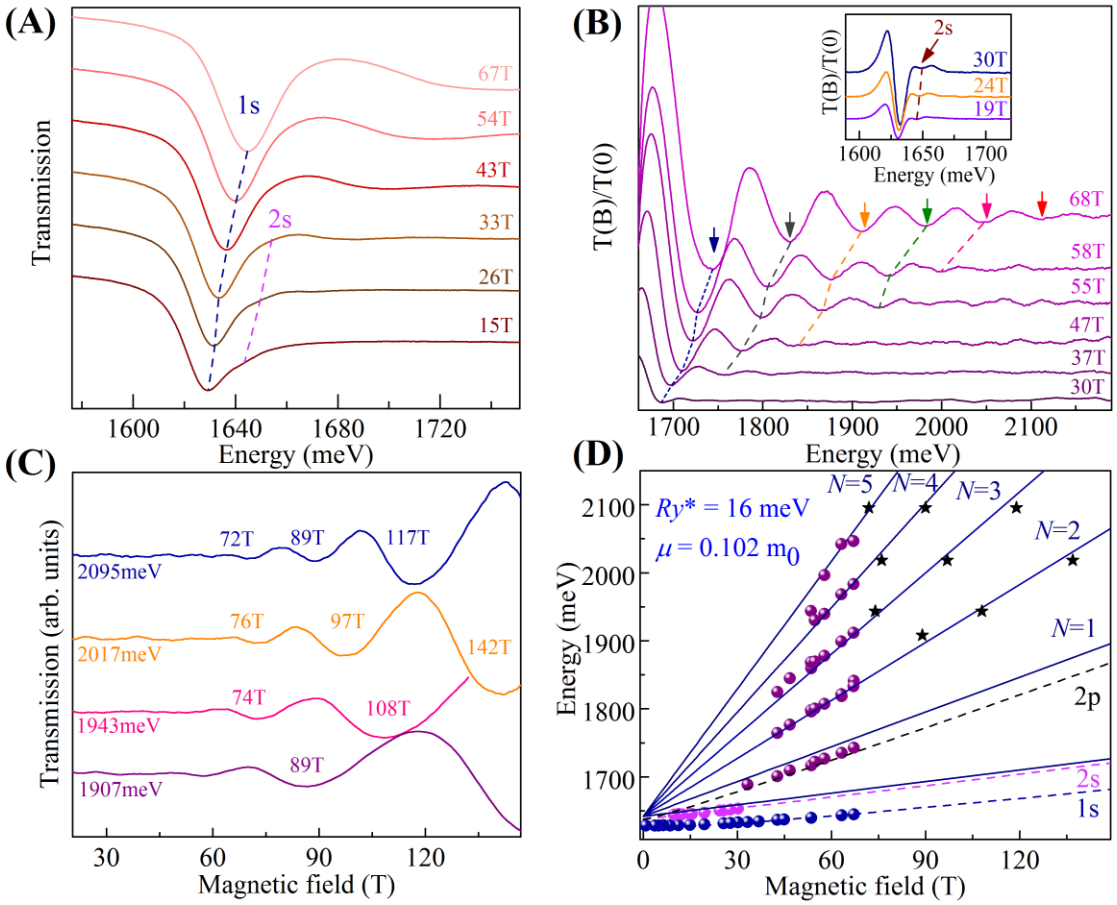

315

316 **Figure 2 Magneto-optical transmission spectrum and fan chart measured at 2 K. A)** Sequence of typical
317 optical transmission spectra of the **LPC** sample measured at the indicated magnetic fields which show the 1s and
318 2s excitonic transitions with increased transmission. **B)** Sequences of the ratios of the transmission spectra in
319 magnetic field $T(B)$ to that measured at zero field $T(0)$. The resonant absorption features of the free carrier
320 Landau levels correspond to minima. **C)** Typical results of the low temperature monochromatic transmission as a
321 function of magnetic field obtained by the short pulse technique. **D)** Fan chart of $CH_3NH_3PbI_3$ for the large grain
322 polycrystalline sample. The circular data points are from long pulse field measurements and star symbol points
323 are collected by short pulse mega-gauss measurements. The solid lines and the dashed lines are the fits to the set
324 of Landau levels and the excitonic transitions, respectively.

325

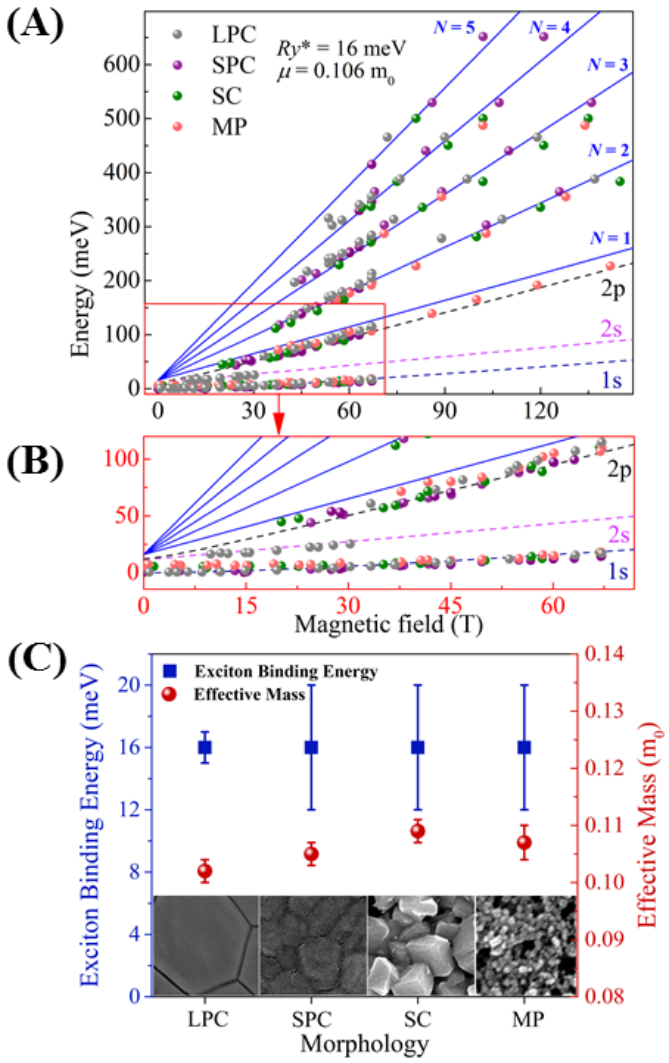

326

327 **Figure 3 Comparison of the excitonic properties of the four different $CH_3NH_3PbI_3$ morphologies. A)**
328 Overlaid fan chart of the LPC, SPC, SC and MP samples. The solid lines and the dashed lines are the fits to the
329 set of Landau levels and the excitonic transitions, respectively. **B)** The zoomed-in plot of the excitonic transitions
330 region of the fan chart in panel **(A)**. **C)** The bottom panel illustrates the change in the Ry^* and μ for the various
331 morphologies.

332

333

334

335

336 **Table 1** Summary of the parameters of the fits to the full Landau fan chart for the four different morphologies of
337 $CH_3NH_3PbI_3$ in the low temperature (2 K), orthorhombic phases. The figures in the brackets are the error
338 estimates of the parameters.

	Size Distribution (nm)	E_g **(meV)**	μ (m_0)	Ry^* **(meV)**
Large Polycrystalline	772(227)	1642(2)	0.102(0.002)	16(1)
Small Polycrystalline	214(57)	1643(2)	0.105(0.002)	16(4)
Small Crystal	291(64)	1639(2)	0.109(0.002)	16(4)
Mesoporous	<50	1638(2)	0.107(0.003)	16(4)

339

Acknowledgements

A.M.S. would like to thank Jincheol Kim for assisting in optimizing the two-step dipping solution-processed samples. The authors acknowledge support from the Australian Government through the Australian Renewable Energy Agency (ARENA) and the Australian Centre for Advanced Photovoltaics (ACAP). The views expressed herein are not necessarily the views of the Australian Government, and the Australian Government does not accept responsibility for any information or advice contained herein. S.D.S. acknowledges funding from the People Programme (Marie Curie Actions) of the European Union's Seventh Framework Programme (FP7/2007–2013) under REA grant agreement number PIOF-GA-2013-622630. This work was partially supported by ANR JCJC project milliPICS, the Région Midi-Pyrénées under contract MESR 13053031, BLAPHENE project under IDEX program Emergence and Programme des Investissements d'Avenir under the program ANR-11-IDEX-0002-02, reference ANR-10-LABX-0037-NEXT. Part of the work has been supported by TERASPEC grant within IDEX Emergence program of University of Toulouse. Zhuo Yang holds a fellowship from the Chinese Scholarship Council (CSC). This work was supported by EPSRC (UK) via its membership to the EMFL (grant no. EP/N01085X/1).

Author Contributions

AMS conceived the idea and designed the experiments with SDS and PP. TY, RB, AP and MA-J fabricated the samples. AMS, SDS and MA-J performed the SEM imaging and XRD measurements. The magneto-optic experiments were performed, under the supervsion of PP, by ZY, AM, AS, KG, JU and NZ, and the data analyzed by ZY. AH-B and MAG supervised AMS, Y-BC supervised AP, OP supervised AM, SDS supervised MA-J, SDS and VB supervised RB. AMS prepared the first draft of the manuscript with technical and editorial inputs from SDS, PP and RJN. All authors contributed to the final version of the manuscript.

Methods

$CH_3NH_3PbI_3$ Perovskite Sample preparation

Large grain polycrystalline film (LPC)

LPC perovskite films were prepared using a methylammonium iodide (CH_3NH_3I) and lead acetate $Pb(Ac)_2 \cdot 3H_2O$ precursor mixture[32]. To generate the perovskite solution, CH_3NH_3I (Dyesol) and $Pb(Ac)_2 \cdot 3H_2O$ were dissolved in anhydrous N,N-dimethylformamide at a 3:1 molar ratio with final concentration of 30 wt%, and the stabilizer hypophosphorous acid (HPA) was added at a molar ratio of 7.5% with respect to Pb(Ac)2 $\cdot$ $3H_2O$. $Pb(Ac)_2 \cdot 3H_2O$ (316512) and HPA (214906) were purchased from Sigma Aldrich. Microscope slides and coverslips were washed sequentially with soap (2% vol. Hellmanex in water), de-ionized water, isopropanol, acetone and finally treated under oxygen plasma for 10 min. The precursor solution was spin-coated at 2,000 r.p.m. for 45 s in a nitrogen-filled glovebox, and the substrates were then dried at room temperature for 10 min before annealing at 100 ºC for 5 min. The samples were then stored in a nitrogen-filled glovebox until used.

Small grain polycrystalline film (SPC)

Soda-lime glass substrates 1 mm thick were purchased from J. Melvin Freed. The substrates were cleaned ultrasonically using soap solution (Helmanex), water, ethanol and iso-propanol for 15 minutes, each.

PbI_2 (99.99%) was purchased from Alfa Aesar and used without further purification. MAI was either synthesised in-house using a common method or else purchased from Dyesol. All the film preparation work was carried out under nitrogen atmosphere.

$CH_3NH_3PbI_3$ films were prepared by the "gas-assisted" method of Huang *et al.* [31]. A 25µL 45 wt% $CH_3NH_3PbI_3$ DMF solution, prepared from PbI_2 and CH_3NH_3I in a molar ratio of 1:1,

was spread on the substrate, on a spin-coater. An 80 L/min stream of nitrogen gas was blown over the film during spinning at 6500 rpm, 2 s after the spinning commenced. The films were annealed at 100°C on a hotplate for 10 min and then cooled to room temperature.

Small crystal sample **(SC)**

Soda-lime glass substrates treatment and precursor solution (PbI_2 and MAI) preparation were similar to that of the small grain polycrystalline film.

$CH_3NH_3PbI_3$ films were prepared by the 2-step method of D'Innocenzo *et al.* [6]. The clean glass substrates were heated on a hotplate at 70° C. A PbI_2 solution in DMF (462 mg/mL) was warmed to 70°C and then spin-coated at 2000 rpm for 60 s. The PbI_2 films were subsequently annealed at 70°C for 30 min. $CH_3NH_3PbI_3$ films with small crystal size were prepared by dipping the PbI_2-coated substrates in a 0.044 M CH_3NH_3I solution in isopropanol at 25°C for 2 minutes. Samples were finally rinsed in anhydrous IPA to remove unreacted CH_3NH_3I.

Mesoporous Al_2O_3 **(MP)**

Unless otherwise specified, all materials were purchased from either Alfa Aesar or Sigma-Aldrich and used as received. The synthesis of CH_3NH_3I was performed using the same previously reported method [31]. The Al_2O_3 (Aldrich, 642991) nanoparticle paste used for characterization measurements was formed by suspending ~ 45 nm particles in a solution of ethanol, terpineol and ethyl cellulose.

Glass substrates were cleaned by sonication in ethanol for 10 mins. The mesoporous Al_2O_3 layer was formed by drop coating approximately 30 $\mu L/cm^2$ of the nanoparticle solution on the glass substrates, which were then annealed at 500 °C for 30 mins. The perovskite precursor solution was formed by mixing stoichiometric amounts of CH_3NH_3I and PbI_2 in a combination of dimethyl sulfoxide (DMSO) and *N*-methyl-2-pyrrolidone (NMP) (7:3 vol) to

form a (46 wt%) concentration solution. Approximately 30 μL/cm^2 of the perovskite precursor solution was applied to the surface of the substrate prior to spin-coating. The films were spin-coated using a two-stage process: 1000 rpm for 5 s using an acceleration of 200 rpm/s, then 6000 rpm for 50 s using an acceleration of 6000 rpm/s. A nitrogen gas flow was introduced after 20 s of the second spin-coating step and sustained for a further 20 s. The perovskite films were then annealed on a hot-plate at 100 °C for a duration of 10 mins.

Mixed-cation Mixed-halide Perovskite Sample preparation

The organic cations were purchased from Dyesol; the lead compounds from TCI; Dimethylformamide (DMF), Dimethyl Sulfoxide (DMSO) and cesium iodide from Sigma Aldrich. The mixed cation lead mixed halide perovskite ($Cs_{0.05}(MA_{0.17}FA_{0.83})_{0.95}Pb(I_{0.83}Br_{0.17})_3$) precursor solutions were prepared by dissolving 1 M FAI, 1.1 M PbI_2, 0.2 M MABr, 0.2 M $PbBr_2$ in a 4:1 (v:v) mixture of anhydrous DMF:DMSO and 1.5 M stock solution of CsI in DMSO was added to the above solution in a 5:95 (CsI:mixture) volume ratio. The perovskite solutions were then spin coated in a two-step program at 1000 and 6000 rpm for 10 and 30 s respectively. During the second step, 50 ul of chlorobenzene was dripped on the spinning substrate 10 s prior to the end. The perovskite film was annealed at 100^o C for 30 min.

SEM imaging

The LPC samples were imaged using a Zeiss Merlin high-resolution scanning electron microscope with a beam energy of 3 kV. The SPC, SC and MP samples were imaged using a FEI Nova NanoSEM 450 scanning electron microscope unit with a beam energy of 15 kV.

Magneto-optical measurement

The magneto transmission measurements were performed combining long pulse magnetic field meausrements and 150 T short duration pulsed magnets.

For the long pulse measurements, the typical duration of the pulse is around 100 ms with the magnetic field up to 66 T. For these measurements, the sample was placed in a liquid helium cryostat. White light from a halogen lamp was used as the excitation source. The light emitted from the lamp was coupled in a 200 μm-diameter multimode fiber, used to illuminate sample. The transmitted light was collected by a 400 μm-diameter multimode fiber and guided to a spectrometer equipped with a liquid nitrogen cooled CCD camera. The typical exposure time was <3 ms, which ensured that the transmission spectra were acquired at an essentially constant magnetic field value.

For very high magnetic field measurements (B<150 T), pulse having a typical duration < 10 μs were generated by a single turn coil system with a bore diameter of 10 mm. A non-conducting helium-flow cryostat was located in the single turn coil. The sample was kept at a temperature of ~5 K. Magneto-transmission measurements were conducted by a using tunable Opical Parametric Oscillator pumped by a Ti:sapphire laser as the light source. A fast (100 MHz) silicon detector and a high speed digital oscilloscope was used for detection.

Reference

1. D. Bi, W. Tress, M. I. Dar, P. Gao, J. Luo, C. Renevier, K. Schenk, A. Abate, F. Giordano, J.-P. Correa Baena, J.-D. Decoppet, S. M. Zakeeruddin, M. K. Nazeeruddin, M. Grätzel and A. Hagfeldt, *Science Advances*, 2016, **2**.
2. M. Saliba, T. Matsui, J.-Y. Seo, K. Domanski, J.-P. Correa-Baena, N. Mohammad K, S. M. Zakeeruddin, W. Tress, A. Abate, A. Hagfeldt and M. Gratzel, *Energy & Environmental Science*, 2016, **9**, 1989-1997.
3. A. Kojima, K. Teshima, Y. Shirai and T. Miyasaka, *Journal of the American Chemical Society*, 2009, **131**, 6050-6051.
4. N. J. Jeon, J. H. Noh, W. S. Yang, Y. C. Kim, S. Ryu, J. Seo and S. I. Seok, *Nature*, 2015, **517**, 476–480.
5. D. P. McMeekin, G. Sadoughi, W. Rehman, G. E. Eperon, M. Saliba, M. T. Hörantner, A. Haghighirad, N. Sakai, L. Korte, B. Rech, M. B. Johnston, L. M. Herz and H. J. Snaith, *Science*, 2016, **351**, 151-155.
6. V. D'Innocenzo, A. R. Srimath Kandada, M. De Bastiani, M. Gandini and A. Petrozza, *Journal of the American Chemical Society*, 2014, **136**, 17730–17733.
7. C. G. Bischak, E. M. Sanehira, J. T. Precht, J. M. Luther and N. S. Ginsberg, *Nano Letters*, 2015, **15**, 4799-4807.
8. Z.-K. Tan, R. S. Moghaddam, M. L. Lai, P. Docampo, R. Higler, F. Deschler, M. Price, A. Sadhanala, L. M. Pazos, D. Credgington, F. Hanusch, T. Bein, H. J. Snaith and R. H. Friend, *Nat Nano*, 2014, **9**, 687-692.
9. M. Saliba, S. M. Wood, J. B. Patel, P. K. Nayak, J. Huang, J. A. Alexander-Webber, B. Wenger, S. D. Stranks, M. T. Hörantner, J. T.-W. Wang, R. J. Nicholas, L. M. Herz, M. B. Johnston, S. M. Morris, H. J. Snaith and M. K. Riede, *Advanced Materials*, 2016, **28**, 923-929.
10. M. A. Green, A. Ho-Baillie and H. J. Snaith, *Nat Photon*, 2014, **8**, 506-514.
11. S. D. Stranks and H. J. Snaith, *Nature Nanotechnology*, 2015, **10**, 391-402.
12. T. Ishihara, *Journal of Luminescence*, 1994, **60-61**, 269–274.
13. M. Hirasawa, T. Ishihara, T. Goto, K. Uchida and N. Miura, *Physica B: Condensed Matter*, 1994, **201**, 427-430.
14. M. Hirasawa, T. Ishihara and T. Goto, *Journal of the Physical Society of Japan*, 1994, **63**, 3870-3879.
15. M. E. Ziffer, J. C. Mohammed and D. S. Ginger, *ACS Photonics*, 2016, **3**, 1060–1068.
16. K. Galkowski, A. Mitioglu, a. miyata, p. plochocka, o. Portugall, G. E. Eperon, J. T.-W. Wang, T. Stergiopoulos, S. D. Stranks, H. Snaith and R. J. Nicholas, *Energy & Environmental Science*, 2016, **9**, 962-970.
17. A. Miyata, A. Mitioglu, P. Plochocka, O. Portugall, J. T.-W. Wang, S. D. Stranks, H. J. Snaith and R. J. Nicholas, *Nat Phys*, 2015, **11**, 582–587.
18. A. M. Soufiani, F. Huang, P. Reece, R. Sheng, A. Ho-Baillie and M. A. Green, *Applied Physics Letters*, 2015, **107**, 231902.
19. Y. Fu, H. Zhu, C. C. Stoumpos, Q. Ding, J. Wang, M. G. Kanatzidis, X. Zhu and S. Jin, *ACS Nano*, 2016, **10**, 7963-7972.
20. S. A. March, D. B. Riley, C. Clegg, D. Webber, X. Liu, M. Dobrowolska, J. K. Furdyna, I. G. Hill and K. C. Hall, *arXiv preprint arXiv:1602.05186*, 2016.
21. A. R. Srimath Kandada and A. Petrozza, *Accounts of Chemical Research*, 2016, **49**, 536–544.
22. G. Grancini, A. R. Srimath Kandada, J. M. Frost, A. J. Barker, M. De Bastiani, M. Gandini, S. Marras, G. Lanzani, A. Walsh and A. Petrozza, *Nat Photon*, 2015, **9**, 695-701.
23. Q. Lin, A. Armin, R. C. R. Nagiri, P. L. Burn and P. Meredith, *Nature Photonics*, 2014, **9**, 106–112.
24. J. Even, L. Pedesseau and C. Katan, *The Journal of Physical Chemistry C*, 2014, **118**, 11566–11572.
25. V. D'Innocenzo, G. Grancini, M. J. P. Alcocer, A. R. S. Kandada, S. D. Stranks, M. M. Lee, G. Lanzani, H. J. Snaith and A. Petrozza, *Nat Commun*, 2014, **5**.
26. L. M. Herz, *Annual Review of Physical Chemistry*, 2016, **67**, 65-89.

27. J. Kim, J. S. Yun, X. Wen, A. M. Soufiani, C. F. J. Lau, B. Wilkinson, J. Seidel, M. A. Green, S. Huang and A. W. Y. Ho-Baillie, *The Journal of Physical Chemistry C*, 2016, **120**, 11262–11267.
28. J. Burschka, N. Pellet, S.-J. Moon, R. Humphry-Baker, P. Gao, M. K. Nazeeruddin and M. Gratzel, *Nature*, 2013, **499**, 316-319.
29. W. S. Yang, J. H. Noh, N. J. Jeon, Y. C. Kim, S. Ryu, J. Seo and S. I. Seok, *Science*, 2015, **348**, 1234-1237.
30. M. Liu, M. B. Johnston and H. J. Snaith, *Nature*, 2013, **501**, 395-398.
31. F. Huang, Y. Dkhissi, W. Huang, M. Xiao, I. Benesperi, S. Rubanov, Y. Zhu, X. Lin, L. Jiang and Y. Zhou, *Nano Energy*, 2014, **10**, 10-18.
32. W. Zhang, S. Pathak, N. Sakai, T. Stergiopoulos, P. K. Nayak, N. K. Noel, A. A. Haghighirad, V. M. Burlakov, D. W. deQuilettes, A. Sadhanala, W. Li, L. Wang, D. S. Ginger, R. H. Friend and H. J. Snaith, *Nat Commun*, 2015, **6**.
33. C. F. Klingshirn, *Semiconductor optics*, Springer, 2007.
34. J. Tilchin, D. N. Dirin, G. I. Maikov, A. Sashchiuk, M. V. Kovalenko and E. Lifshitz, *ACS Nano*, 2016, **10**, 6363-6371.
35. P. C. Makado and N. C. McGill, *Journal of Physics C: Solid State Physics*, 1986, **19**, 873.
36. G. Mahan, *Proc. 1971 Antwerp Advanced Study Inst*, 1972.
37. D. Li, G. Wang, H.-C. Cheng, C.-Y. Chen, H. Wu, Y. Liu, Y. Huang and X. Duan, *Nat Commun*, 2016, **7**.
38. A. Osherov, E. M. Hutter, K. Galkowski, R. Brenes, D. K. Maude, R. J. Nicholas, P. Plochocka, V. Bulović, T. J. Savenije and S. D. Stranks, *Advanced Materials*, 2016, **28**, 10757-10763.
39. K. Galkowski, A. A. Mitioglu, A. Surrente, Z. Yang, D. K. Maude, P. Kossacki, G. E. Eperon, J. T. W. Wang, H. J. Snaith, P. Plochocka and R. J. Nicholas, *Nanoscale*, 2017, **9**, 3222.
40. M. R. Filip, G. E. Eperon, H. J. Snaith and F. Giustino, *Nature communications*, 2014, **5**.
41. M. A. Pérez-Osorio, R. L. Milot, M. R. Filip, J. B. Patel, L. M. Herz, M. B. Johnston and F. Giustino, *The Journal of Physical Chemistry C*, 2015, **119**, 25703-25718.
42. A. M. A. Leguy, A. R. Goni, J. M. Frost, J. Skelton, F. Brivio, X. Rodriguez-Martinez, O. J. Weber, A. Pallipurath, M. I. Alonso, M. Campoy-Quiles, M. T. Weller, J. Nelson, A. Walsh and P. R. F. Barnes, *Physical Chemistry Chemical Physics*, 2016, **18**, 27051-27066.
43. Y. Yamada, T. Nakamura, M. Endo, A. Wakamiya and Y. Kanemitsu, *IEEE Journal of Photovoltaics*.
44. C. Motta, P. Mandal and S. Sanvito, *Physical Review B*, 2016, **94**, 045202.
45. M. B. Price, J. Butkus, T. C. Jellicoe, A. Sadhanala, A. Briane, J. E. Halpert, K. Broch, J. M. Hodgkiss, R. H. Friend and F. Deschler, *Nature Communications*, 2015, **6**.
46. Y. Yang, D. P. Ostrowski, R. M. France, K. Zhu, J. van de Lagemaat, J. M. Luther and M. C. Beard, *Nat Photon*, 2015, **10**, 53–59.
47. N. Sestu, M. Cadelano, V. Sarritzu, F. Chen, D. Marongiu, R. Piras, M. Mainas, F. Quochi, M. Saba, A. Mura and G. Bongiovanni, *The Journal of Physical Chemistry Letters*, 2015, **6**, 4566-4572.